First-principles calculation of lattice thermal conductivities of α-, β-, and γ-Si_3N_4

Kazuyoshi Tatsumi,[1,2,*] Atsushi Togo,[2] and Isao Tanaka[2,3,4]

[1] *Institute of Materials and Systems for Sustainability, Nagoya University, Chikusa, Nagoya 464-8603, Japan*
[2] *Center for Elements Strategy Initiative for Structural Materials, Kyoto University, Sakyo, Kyoto 606-8501, Japan*
[3] *Department of Materials Science and Engineering, Kyoto University, Sakyo, Kyoto 606-8501, Japan*
[4] *Nanostructures Research Laboratory, Japan Fine Ceramics Center, Atsuta, Nagoya 456-8587, Japan*

Lattice thermal conductivities of α-, β- and γ-Si_3N_4 phases are investigated from *ab-initio* anharmonic lattice dynamics, within the single-mode relaxation-time approximation of the linearized phonon Boltzmann transport equation. At 300 K, the lattice thermal conductivity of β-Si_3N_4 is calculated as $\kappa_{xx} = 73$ and $\kappa_{zz} = 199$ (in units of $Wm^{-1}K^{-1}$), that is consistent with the reported experimental values of 69 and 180, respectively. For α-Si_3N_4, $\kappa_{xx} = 68$ and $\kappa_{zz} = 100$ are obtained. The difference of anisotropy between these phases is originated from their characteristic difference in the phonon band structures, closely related to the crystal structures. In α-Si_3N_4, acoustic-mode phonons below 6 THz are the main heat carriers. In β-Si_3N_4, the phonon modes up to 12 THz contribute to the lattice thermal conductivity. In γ-Si_3N_4, $\kappa = 77$ is obtained. The distribution of phonon mode contributions to lattice thermal conductivity with respect to phonon frequency is found to closely resemble that for κ_{xx} of β-Si_3N_4 although the phonon lifetimes of γ-Si_3N_4 are twice shorter than those of β-Si_3N_4.

I. INTRODUCTION

Several nitride insulators are known to exhibit high thermal conductivities and are important for heat transfer materials at elevated temperatures. For example, Slack *et al.*[1] reported that wurtzite-type AlN has thermal conductivity exceeding 100 $Wm^{-1}K^{-1}$. Si_3N_4 has become another promising thermal conductive insulator because its thermal conductivity has been improved up to 177 $Wm^{-1}K^{-1}$ by using the advanced ceramic technologies related to the densification and microstructure control.[2–5] Since the Si_3N_4 ceramics also exhibit high mechanical strength at elevated temperatures, they are regarded as ideal materials for the use in various applications, such as engine components, gas turbines, and heat sink substrates of power semiconductor devices.

At atmospheric pressure, Si_3N_4 has two phases, α and β, which are generally considered as low- and high-temperature phases, respectively.[2,6,7] Their crystal structures belong to the space groups of P31c and $P6_3/m$, respectively.[8,9] These structures have different stacking manners of equivalent basal layer structures composed of SiN_4 tetrahedra.[10] In Fig. 1 these layer structures are depicted from the principal axis direction. They are denoted as A, B, C, and D in the α phase and A and B in the β phase, respectively. The stacking manners are thus as ABCDABCD.. and ABAB.., respectively. The α phase has additional two layer structures of C and D, which are related to A and B by the c glide operation.[10] Along this direction the lattice constant of the α phase is approximately twice longer than that of the β phase.

The experimental thermal conductivities[2–5,12] of the Si_3N_4 polymorphs were measured on the polycrystalline bulk samples. These values were significantly affected by the lattice defects, impurities, shapes and orientations of the constituent crystal grains;[6] the thermal conductivity intrinsic to defect-free Si_3N_4 has not been established. As an experimental approach for it, Li *et al.*[13] applied the high-resolution thermoreflectance microscopy on single β-Si_3N_4 grains in a ceramic sample. Their analyzed thermal conductivity was 69 and 180 $Wm^{-1}K^{-1}$ along the a and c axes, respectively. These values re-

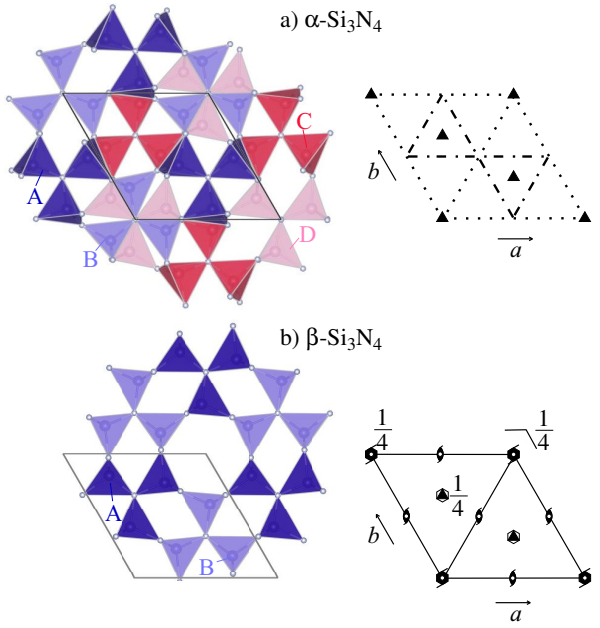

FIG. 1. (color online) Crystal structures of α- and β-Si_3N_4. Stacking of SiN_4 tetrahedron layers are shown in left. (a) ABCDABCD.. for α-Si_3N_4. (b) ABAB.. for β-Si_3N_4. Space group diagrams[11] in P31c (α-Si_3N_4) and $P6_3/m$ (β-Si_3N_4) are shown in right.

spectively correspond to the xx and zz elements of the lattice thermal conductivity tensor $\boldsymbol{\kappa}$. We consider the anisotropy of $\kappa_{zz}/\kappa_{xx} \sim 3$ is relatively large. Theoretically, Hirosaki *et al.*[6] estimated the $\boldsymbol{\kappa}$ by applying the Green-Kubo formulation to the molecular dynamics (MD) method with the interatomic potentials proposed by Vashishta *et al.*[14]. They calculated κ_{xx} and κ_{zz} of α-Si_3N_4 as 105 and 225 $Wm^{-1}K^{-1}$, and those of β-Si_3N_4 as 170 and 450 $Wm^{-1}K^{-1}$, respectively. The ratio κ_{zz}/κ_{xx} in β-Si_3N_4 agreed well with the experimental ratio; the κ_{xx} and κ_{zz} overestimated the experimental $\boldsymbol{\kappa}$ more than twice.

Based on a first principles calculation and Boltzmann transport theory[15], Togo *et al.* recently calculated $\boldsymbol{\kappa}$ of many polymorphs of the zincblende- and wurtzite-type structures. Their crystal structures have stacking manners of the densest atom planes as ABCABC.. and ABAB.., respectively. The different stacking manners merely altered the $\boldsymbol{\kappa}$ as well as the phonon linewidths and phonon density of states.[15] On the other hand, the previous MD results presented that the different stacking manners between the α and β phases altered the $\boldsymbol{\kappa}$ largely. This has not been explained through their phonon properties. It is interesting to investigate this based on the first principles anharmonic phonon calculation.

In addition to the α and β phases, a cubic spinel phase (γ-Si_3N_4) is known to form upon compression and in-situ heating.[16,17] The reported transition pressures are scattered from 10 to 36 GPa depending on the experimental conditions.[18] The γ phase is experimentally quenched to atmospheric pressure and room temperature. Its thermal conductivity has not been experimentally reported; it has been estimated by the Slack model.[19]

The present study aims to qualitatively understand the lattice thermal conductivity tensors among the three Si_3N_4 phases by means of the first principles approach. We calculate the $\boldsymbol{\kappa}$ of the γ phase as well, for systematic understanding. After the methodology section, we examine the validity of the present results first. Our calculated thermal properties are compared with the available experimental and theoretical references. Then we investigate the characteristic behaviors of the $\boldsymbol{\kappa}$ in detail on the basis of the phonon band structures and phonon linewidths.

II. COMPUTATIONAL PROCEDURES

A. Lattice thermal conductivity calculation

The lattice thermal conductivities were calculated by solving the linearized Boltzmann transport equation (LBTE) within the single-mode relaxation time approximation (single-mode RTA). The harmonic phonon states and lattice thermal conductivities were calculated with phonopy[20] and phono3py[15] software packages, respectively. We also tried the direct-solution of LBTE[21] and leave its calculated $\boldsymbol{\kappa}$ values in the following section. The differences between the $\boldsymbol{\kappa}$ calculated by the single-mode RTA and the direct solution were found minor for our discussion. Therefore we limited our research to use the single-mode RTA to take advantage of its intuitive closed form of $\boldsymbol{\kappa}$.

In the following sections, we denote a phonon mode by $\lambda = (\mathbf{q}, p)$ with the set of the phonon wave vector $\mathbf{q}$ and band index p and $-\lambda \equiv (-\mathbf{q}, p)$. The relaxation time due to phonon-phonon scattering was obtained as half the reciprocal of linewidth, $\tau_{\lambda,\text{ph-ph}} = (2\Gamma_\lambda)^{-1}$, where the linewidth that we employed in this study is as follows:

$$\Gamma_\lambda = \frac{18\pi}{\hbar^2} \sum_{\lambda'\lambda''} \left|\Phi_{-\lambda\lambda'\lambda''}\right|^2 \times \{(n_{\lambda'} + n_{\lambda''} + 1)\delta(\omega_\lambda - \omega_{\lambda'} - \omega_{\lambda''}) + (n_{\lambda'} - n_{\lambda''})\left[\delta(\omega_\lambda + \omega_{\lambda'} - \omega_{\lambda''}) - \delta(\omega_\lambda - \omega_{\lambda'} + \omega_{\lambda''})\right]\}. \quad (1)$$

Here ω_λ is the harmonic phonon frequency of the phonon mode λ, $n_\lambda = [\exp(\hbar\omega_\lambda/k_B T) - 1]^{-1}$ is the Bose-Einstein distribution at temperature T, and $\Phi_{\lambda\lambda'\lambda''}$ denotes the three-phonon-scattering strength. $\Phi_{\lambda\lambda'\lambda''}$ was obtained by usual coordinate transformation of third-order force constants from direct space to phonon space.[15] The second- and third-order real-space force constants were obtained from the *ab-initio* calculation, whose details are written in the next section.

In order to more realistically compare the calculated $\boldsymbol{\kappa}$ with the measured thermal conductivities, the isotopic scattering effect due to the natural isotope distribution was taken into account according to the second-order perturbation theory.[22] Using the relaxation times of the phonon-phonon scattering and isotopic scattering, $\tau_{\lambda,\text{ph-ph}}$ and $\tau_{\lambda,\text{iso}}$, the total relaxation time for a phonon mode, τ_λ, was calculated by assuming Matthiessen's rule, $1/\tau_\lambda = 1/\tau_{\lambda,\text{ph-ph}} + 1/\tau_{\lambda,\text{iso}}$.

The experimental thermal conductivities in the Si_3N_4 system were measured on the polycrystalline samples and not measured from any single crystals. The conductivities measured at a polycrystalline area were affected by various lattice defects within it, such as grain boundaries, impurities, and vacancies. We crudely took them into account by a relaxation time $\tau_{\lambda,\text{bs}} = L/|\mathbf{v}_\lambda|$ of a phonon boundary scattering model, where $\mathbf{v}_\lambda = \nabla_{\mathbf{q}}\omega_\lambda$ is the group velocity and L a parameter regarding to the boundary mean free path. We consider $\tau_{\lambda,\text{bs}}$ as a variable parameter and partly include it to the calculated $\boldsymbol{\kappa}$ according to Matthiessen's rule.

The closed form of $\boldsymbol{\kappa}$ within RTA was obtained via

$$\boldsymbol{\kappa}(T) = \frac{1}{N_{\mathbf{q}}\Omega} \sum_\lambda \tau_\lambda(T)\mathbf{v}_\lambda \otimes \mathbf{v}_\lambda c_\lambda(T), \quad (2)$$

where $N_{\mathbf{q}}$ is the number of $\mathbf{q}$-points, Ω is the unit cell volume, and c_λ is the mode heat capacity. To analyze $\boldsymbol{\kappa}$ in

detail, we calculate the cumulative thermal conductivity:

$$\boldsymbol{\kappa}^{\mathrm{c}}(\omega) = \frac{1}{N_{\mathbf{q}}\Omega}\int_0^{\omega}\sum_{\lambda}\tau_{\lambda}(T)\mathbf{v}_{\lambda}\otimes\mathbf{v}_{\lambda}c_{\lambda}(T)\delta(\omega'-\omega)d\omega', \tag{3}$$

and its derivative $\frac{\partial\boldsymbol{\kappa}^{\mathrm{c}}(\omega)}{\partial\omega}$ to see the phonon mode contributions to $\boldsymbol{\kappa}$.

B. Computational details

The force constants required for the lattice dynamics were calculated using the first-principles projector augmented wave method[23] (VASP code[24–26]). The generalized gradient approximation (GGA) parameterized by Perdew, Burke, and Ernzerhof[27] was used for the exchange correlation potential. A plane wave energy cutoff of 500 eV was employed. The crystal structures were optimized for 0 K and 0 GPa until the residual forces acting on the constituent atoms were less than 10^{-6} eV/Å. Here the temperature and pressure were considered only for the electronic system and the zero point lattice vibration was not considered. The calculated lattice parameters were $a = 7.808$ Å and $c = 5.659$ Å for the α phase, $a = 7.660$ Å and $c = 2.925$ Å for the β phase, and $a = 7.787$ Å for the γ phase, which agree with the experimental data[8,9,28] within +0.7 % errors. The lattice volume optimized with the local density approximation (LDA)[29] for the exchange correlation potential was, for β-Si_3N_4, 3 % smaller than the volume optimized with GGA, which is a typical volume contraction of LDA. κ_{xx} and κ_{zz} calculated with LDA were larger by 0.3 and 2.6 % than those calculated with GGA. For our discussion, these differences are enough small, therefore the impact of choice of exchange correlation potential is considered to be minor in our study.

The force constants were calculated by the finite difference approach[30]. For this calculation, we adopted following supercells: $1\times1\times2$, $1\times1\times3$, and $1\times1\times1$ supercells of the conventional unit cells for the calculations of the third-order force constants of α, β, and γ-Si_3N_4, respectively, and $3\times3\times4$, $3\times3\times8$ and $2\times2\times2$ for those of the second-order force constants. The length of the induced atomic displacements was set to 0.03 Å. Table I shows the $\boldsymbol{\kappa}$ calculated with several different sets of the supercells, indicating that our calculated $\boldsymbol{\kappa}$ is reasonably converging with respect to the size of the supercells.

Uniform $\mathbf{k}$-point sampling meshes of $4\times4\times2$, $4\times4\times3$, and $3\times3\times3$ were employed for the calculations of the third-order force constants of the α, β, and γ phases. For the α and β phases the center of the a^*b^* plane was sampled while the center on the c^*-axis was not. For the γ phase, non-Γ center mesh was used. For the calculations of the second-order force constants, the Γ-point was only sampled for the α and β phase and the only one $\mathbf{k} = (0.5, 0.5, 0.5)$ point was sampled for the γ phase. The $\mathbf{q}$-point sampling meshes of $10\times10\times14$, $10\times10\times26$, and $12\times12\times12$ were employed to calculate $\boldsymbol{\kappa}$ in Eq. (2) for the α, β, and γ phases.

TABLE I. Calculated lattice thermal conductivities of α-, β-, and γ-Si_3N_4 ($WK^{-1}m^{-1}$) at 300 K with respect to several combinations of supercell sizes.

Phase	Supercell (# of atoms)		LTC	
	3rd force constants	2nd force constants	xx	zz
α	$1\times1\times1$ (28)	$1\times1\times1$ (28)	37	57
	$1\times1\times2$ (56)	$1\times1\times2$ (56)	41	79
	$1\times1\times1$ (28)	$2\times2\times2$ (224)	55	81
	$1\times1\times2$ (56)	$2\times2\times2$ (224)	67	95
	$1\times1\times2$ (56)	$2\times2\times3$ (336)	68	97
	$1\times1\times2$ (56)	$3\times3\times4$ (1008)	68	100
β	$1\times1\times2$ (28)	$1\times1\times2$ (28)	44	173
	$1\times1\times2$ (28)	$2\times2\times4$ (224)	76	208
	$1\times1\times3$ (42)	$2\times2\times4$ (224)	71	194
	$1\times1\times3$ (42)	$2\times2\times5$ (280)	72	196
	$1\times1\times3$ (42)	$3\times3\times8$ (1008)	73	199
γ	$1\times1\times1$ (56)	$1\times1\times1$ (56)	72	
	$1\times1\times1$ (56)	$2\times2\times2$ (448)	77	
	$1\times1\times1$ (56)	$3\times3\times3$ (56)	79	

Non-analytical term correction[31] was applied to the second-order force constants to take into account the long range Coulomb forces present in ionic crystals. For the correction, static dielectric constants and Born effective charges were calculated by using the density functional perturbation theory as implemented in the VASP code[32,33].

We examined the effect of lattice thermal expansion on $\boldsymbol{\kappa}$. For this, we calculated $\boldsymbol{\kappa}$ for several finite temperatures with the crystal structures optimized for the corresponding temperatures within the quasi-harmonic approximation (QHA)[34]. These $\boldsymbol{\kappa}$ were different from those calculated for the same temperatures with the structure optimized for 0 K. We consider these differences as the effect of lattice thermal expansion. We found the $\boldsymbol{\kappa}$ differences for T=300, 600, 900, 1200, and, 1500 K within 1 %, similarly, in the case of Si and Ge[35]. For the present study, these differences are negligible and for finite temperatures we adopted the $\boldsymbol{\kappa}$ calculated with the structure optimized for 0 K.

In addition, we calculated the volumetric thermal expansion coefficients. Their comparison with the experimental coefficients is useful to validate the present thermal conductivity calculation, because the thermal expansion is originated from the anharmonicity of the interatomic potential as well as $\boldsymbol{\kappa}$. The calculated coefficients of the α, β, and γ phases were 4.31×10^{-6}, 4.19×10^{-6} K^{-1}, and 1.13×10^{-5} for 300 K, while the experimental values[36,37] are 3.75×10^{-6} , 3.55×10^{-6} K^{-1}, and 9.48×10^{-6} K^{-1}. The calculation systematically overestimated the experimental values, but reproduced the experimental tendencies, including that the α phase has

a slightly larger thermal expansion coefficient than the β phase. This supports that the present calculation enables us to qualitatively compare the calculated $\boldsymbol{\kappa}$ among the Si_3N_4 phases.

In order to compare the microscopic phonon properties among the three phases at the same conditions, those results calculated at 0 GPa are shown and discussed. For the γ phase, this means that we assume the condition of a virtually quenched γ phase at 0 GPa from the high pressure. To examine the analytical continuity of the properties with respect to pressures, we calculated $\boldsymbol{\kappa}$ of the γ phase at 10, 20, and 40 GPa as shown in Fig. 9. The phenomenological behaviour of linear dependence of $\boldsymbol{\kappa}$ with respect to pressure was reproduced as similar to Ref. 38. The slope was 2.89 $\mathrm{Wm^{-1}K^{-1}GPa^{-1}}$ for the γ phase. By this dependence, we consider that the microscopic values are also varied smoothly with the pressure and those at 0 GPa are valuable to be compared with the corresponding values of the α and β phases.

C. Direct solution of LBTE

The merit to employ the single-mode RTA for thermal conductivity calculation is the closed form, by which we can intuitively understand the qualitative character of $\boldsymbol{\kappa}$ in terms of the phonon-mode specific properties. The microscopic understanding of the full solution of LBTE is still under the development[39] and the microscopic picture based on collective phonons[40] will require more complicated investigation.

It is known that the single-mode RTA solution of LBTE often underestimates the full solution.[35,41] To check the underestimation, we calculated $\boldsymbol{\kappa}$ of the α and β phases by a direct solution of LBTE[21], which is one of the methods of LBTE full solutions. Their κ_{xx} and κ_{zz} without the isotope effect were 69 and 102 $\mathrm{Wm^{-1}K^{-1}}$ for the α phase and 76 and 238 $\mathrm{Wm^{-1}K^{-1}}$ for the β phase, respectively, while the corresponding single-mode RTA values were 70 and 102 $\mathrm{Wm^{-1}K^{-1}}$ for the α phase and 76 and 210 $\mathrm{Wm^{-1}K^{-1}}$ for the β phase. The κ_{zz} of the direct solution in the β phase was 13 % larger than that of the single-mode RTA solution. Since the differences in $\boldsymbol{\kappa}$ between the LBTE solutions are not significant, we expect the physics on those lattice thermal conductivities is well understood within the single-mode RTA in the current level of our interest. Therefore, we discuss the lattice thermal conductivities calculated by the single-mode RTA solution.

III. RESULTS AND DISCUSSION

A. Lattice thermal conductivities

Table II shows the calculated $\boldsymbol{\kappa}$ for 300 K. β-Si_3N_4 has a markedly more anisotropic $\boldsymbol{\kappa}$ than α-Si_3N_4. The directional averages $\sum_i \kappa_{ii}/3$ are 79, 115, and 77 $\mathrm{Wm^{-1}K^{-1}}$ for the α, β, and γ phases, respectively. The value of the γ phase is similar to that of the α phase, in spite of comparatively large difference among the bulk moduli (B) that are also shown in Table II.

TABLE II. Calculated thermal conductivities of α-Si_3N_4 (trigonal), β-Si_3N_4 (trigonal), and γ-Si_3N_4 (cubic) at 300 K in units of $\mathrm{Wm^{-1}K^{-1}}$, compared with the experimental and theoretical reference data. Theoretical bulk moduli B in units of GPa, calculated by the authors by using the present band method, are presented in the fourth column.

	This work			Ref. Theo.			Ref. Expt.	
	κ_{xx}	κ_{zz}	B	κ	κ_{xx}	κ_{zz}	κ_{xx}	κ_{zz}
α-Si_3N_4	68	100	224	70[a]	105[b]	225[b]	-	-
β-Si_3N_4	73	199	237	250[a]	170[b]	450[b]	69[c]	180[c]
γ-Si_3N_4	77	-	296	80[a]	-	-	-	-

[a] Ref. 19, Slack model.
[b] Ref. 6, molecular dynamics (Green-Kubo).
[c] Ref. 13, single crystalline grains of poly-crystals.

Table II also lists the previously reported experimental[13] and theoretical[6] $\boldsymbol{\kappa}$ for the references. The theoretical results[19] of the Slack model, which do not include the anisotropy in $\boldsymbol{\kappa}$, are shown as κ in Table II. For the β phase, compared to the $\boldsymbol{\kappa}$ of the molecular dynamics[6], our $\boldsymbol{\kappa}$ agrees better with the experimental $\boldsymbol{\kappa}$. Also, compared to the κ of the Slack model, our directional average $\sum_i \kappa_{ii}/3$ is much closer to the experimental average.

Fig. 2 shows the theoretical $\boldsymbol{\kappa}$ of the α and β phases as a function of T, together with the reference experimental data[5,12]. The experimental thermal conductivities for a series of temperatures were measured on polycrystalline areas by the laser flash method. These thermal conductivities (denoted as $\kappa_{\mathrm{polycrystal}}$) cannot be directly compared with the calculated intrinsic $\boldsymbol{\kappa}$ because they largely depended on the microstructure of the samples: They were deviated from the simple directional averages of the intrinsic κ_{ii}, depending on the shapes of the crystal grains. We treated this effect by using a parameter $0 \leq w \leq 1$ and fitting the quantity $w\kappa_{xx} + (1-w)\kappa_{zz}$ to the experimental $\kappa_{\mathrm{polycrystal}}$ by the least squares method. We regard it as theoretical $\kappa_{\mathrm{polycrystal}}$.

In Fig. 2, the κ_{ii} calculated without $\tau_{\lambda,\mathrm{bs}}$ are nearly proportional to T^{-1} because n_λ in Eq. (1) can be reduced to $\frac{k_B T}{\hbar\omega_\lambda} - \frac{1}{2}$. In Fig. 2-a, the experimental $\kappa_{\mathrm{polycrystal}}$ of a chemically vapor-deposited α-Si_3N_4 sample[12] is not proportional to T^{-1} and intersects the theoretical κ_{ii}. Thus w does not adjust the theoretical $\kappa_{\mathrm{polycrystal}}$ to the experimental $\kappa_{\mathrm{polycrystal}}$. The full solution of LBTE would negligibly cure the disagreement. Including the simple phonon lifetime of boundary scattering, $\tau_{\lambda,\mathrm{bs}} = L/|\mathbf{v}_\lambda|$, into the total phonon lifetime could not explain the discrepancy as well. A L value of 0.6 μm, which was much smaller than the experimental grain size[12] of 10 μm, decreased the theoretical κ_{ii} in the low temperature side toward the experimental values, but the κ_{ii} in the high

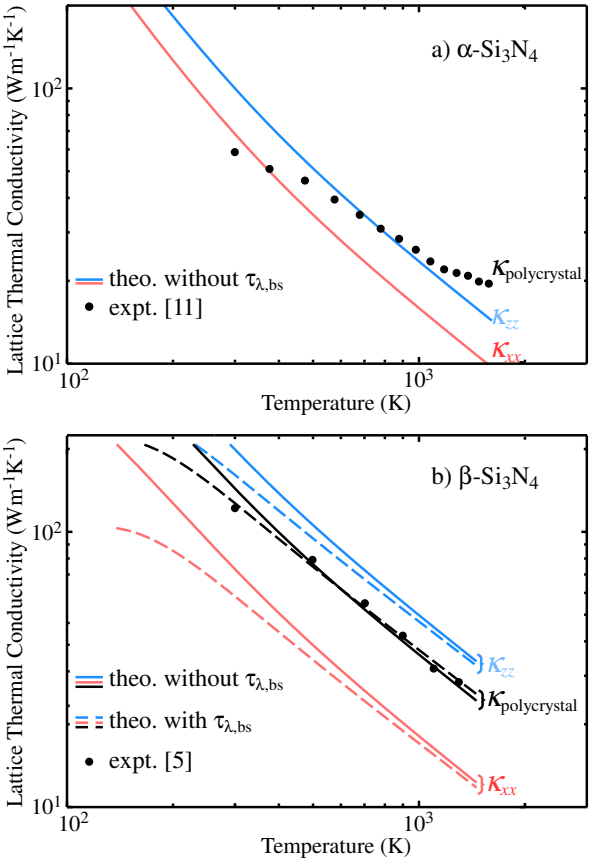

FIG. 2. (color online) Temperature dependences of thermal conductivities for α- and β-Si_3N_4. For β-Si_3N_4, theoretical conductivities with the boundary scattering effect are shown by broken lines. Theoretical $\kappa_{\rm polycrystal}$ (see in text) for the β-Si_3N_4 sample are also shown to be compared with the experimental conductivities.

temperature side continued to be severely smaller than the experimental values. At present, the reason for the discrepancy between the theoretical and experimental behaviors is unclear. Although the crystal structure of the experimental sample was characterized as α-Si_3N_4, significant lattice defects existed in the sample as pointed out by Hirosaki *et al.*[6] and the simple phonon boundary scattering model may fail to describe their effects on the $\kappa_{\rm polycrystal}$.

For the β phase, the experimental $\kappa_{\rm polycrystal}$ is located in-between the theoretical κ_{xx} and κ_{zz} curves, being nearly proportional to T^{-1}. Simple directional averages of the theoretical κ_{ii} slightly underestimate these experimental values. This is understood from the fact that the microstructure was controlled to increase the $\kappa_{\rm polycrystal}$, and the crystalline grains were selectively grown along the c axis of the most conductive direction.[5] The theoretical $\kappa_{\rm polycrystal}$ was fit well with $w = 0.44$ to the experimental. For the effects of lattice defects most of which were grain boundaries, we included $\tau_{\lambda,\rm bs}$ with $L = 0.6$ μm to further fit the theoretical curve ($w = 0.33$) to the experimental data. The L value is slightly smaller than the average grain size[5] of 2 μm in the experiment, the discrepancy presumably explained by the other existing lattice defects than the grain boundaries.

B. Dispersion curves

Figure 3 shows the phonon band diagrams of the three Si_3N_4 phases. The branches are classified according to their symmetry group, by using different colors and line styles. The full and broken lines are used for degenerate and non-degenerate modes, respectively. The entire band diagrams are almost identical to those reported earlier[18,42] and thus not shown. Here we investigate the frequency gradients, the group velocities projected on the paths. We especially focus on their anisotropy in the α and β phases. This was not investigated by the previous works.

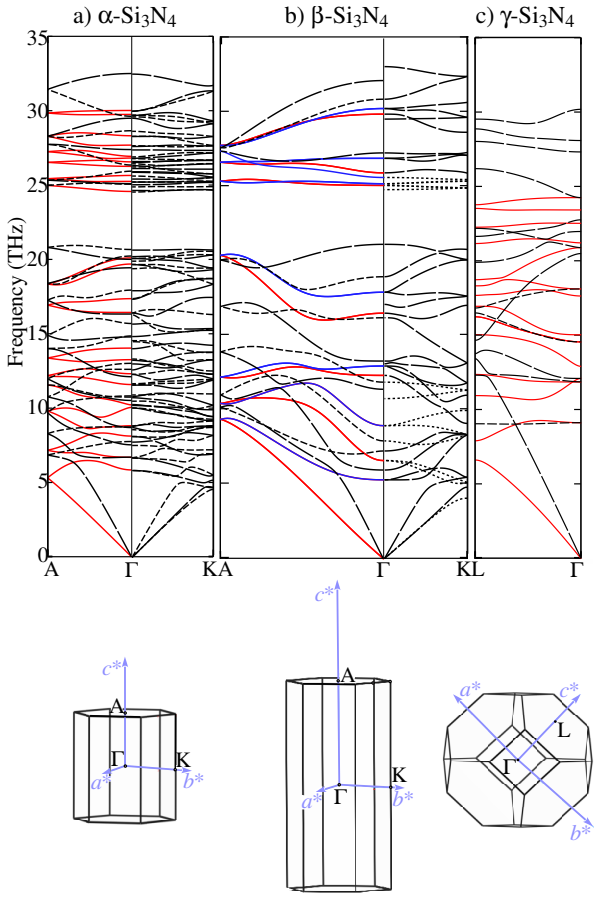

FIG. 3. (color online) Calculated phonon band diagrams (top) for three Si_3N_4 phases and Brillouin-zones (bottom).

Because the α phase unit cell contains two times more basal layer structures than the β phase unit cell, the edge of the α phase Brillouin zone in the stacking direction A is half as far as that of the β phase. The number of

phonon branches in the α phase are twice more than that in the β phase. In general, phonon branches being adjacent in frequency and belonging to the same symmetry group show a band gap, and an anticrossing occurs when they are close to each other. If we regard the α phase lattice as a superlattice of the β phase lattice, then the phonon branches of the α phase in Fig. 3-a are produced by folding the phonon branches of the β phase at the perpendicular bisector plane of ΓA. Taking for example the folding of the acoustic phonon branch, in Fig. 3-a, an upper branch belonging to the same symmetry group is located very close in frequency, inevitably entailing an anticrossing and a band gap between them. This explains why the folded branch, which is degenerate at A with the acoustic branch due to the non-symmorphic symmetry, can not increase its frequency as it goes back on ΓA in Fig. 3-a. The band gap and anticrossing creations are reported in the theoretical study on lattice thermal conductivities of GaAs/AlAs superlattices.[43] It is interesting that the effects occur, in the present system, due to the stacking manners of the unit structures composed of the same elements.

As a result, in Fig. 3-a, the acoustic phonon branches increase their frequencies similarly between these paths. In contrast, the corresponding frequencies in Fig. 3-b increase much more from Γ to A than from Γ to K. The anisotropic frequency increments indicate the anisotropic $\mathbf{v}_\lambda$. Compared with the α and γ phases, the β phase shows significantly steep slopes for the low frequency optical phonon branches on ΓA. This indicates that $v_{\lambda,z}$ of these phonon modes are large. The anisotropic $\mathbf{v}_\lambda$ of the acoustic and low frequency optical phonons will be investigated further in the following sections.

In the γ phase, the longitudinal acoustic branches keep linear dispersion at higher frequencies than in the other phases. The gradients of ω_λ are largest among the three phases, as expected by the largest B.

C. ω_λ contour map on reciprocal plane

We investigate the anisotropy in the $\mathbf{v}_\lambda$ of α- and β-Si_3N_4 by using another geometry, that is, a cross-section of the Brillouin-zone. Fig. 4 shows contour maps of ω_λ on the b^*c^* plane. We show the maps for the four lowest-frequency bands, because they contribute significantly to the $\boldsymbol{\kappa}$, which will be confirmed in the next section. There were negligible differences between the distributions on the b^*c^* plane and the other planes containing the c^* axis. Thus we select the b^*c^* plane as a representative. In the α phase, the ω_λ distributions and thus $\mathbf{v}_\lambda$ are nearly isotropic. In the β phase, the contours are rather parallel to the b^* axis and thus the $\mathbf{v}_\lambda$ tend to orient toward the c^* axis direction. This confirms the large anisotropy of the $\mathbf{v}_\lambda$ of the β phase for the acoustic and low-frequency optical phonon branches.

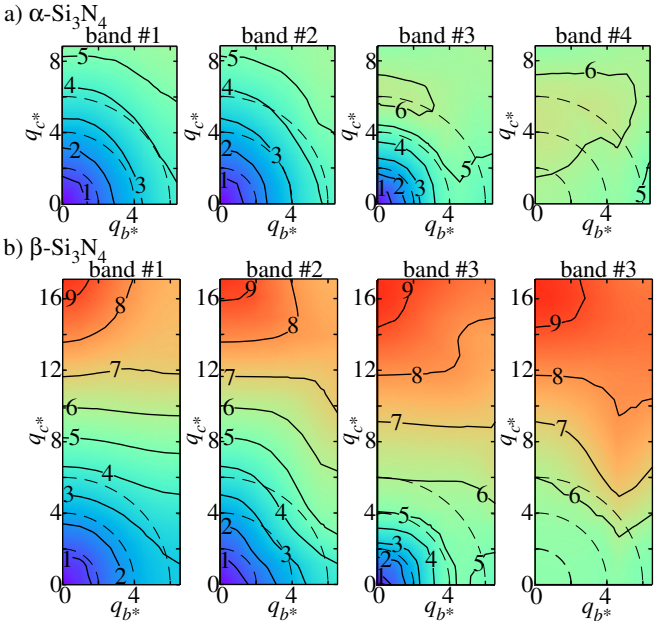

FIG. 4. (color online) Contour maps of phonon frequency (THz) on the b^*c^* planes of Brillouin-zones. The coordination in the reciprocal plane are in units of 10^{-2} Å^{-1}. The maps for the four lowest-frequency phonon modes are shown. The frequency landscapes are formed by simply connecting the frequencies of the same band indices, assigned by ascending order of frequency at the respective $\mathbf{q}$ points.

D. Frequency-distributions of phonon properties

We have investigated in the previous two sections the anisotropy in the $\mathbf{v}_\lambda$, which may explain the anisotropy in the $\boldsymbol{\kappa}$. Here we examine which phonon frequencies and which terms in the RTA closed form characterize the behaviors of the present $\boldsymbol{\kappa}$. In the following, we disregard the term of mode heat capacity since it is approximately constant for 300 K. The effects of the isotope scattering and boundary scattering are not considered for simplicity. For the investigation, the cumulative thermal conductivity, $\boldsymbol{\kappa}^c(\omega)$ in Eq.(3), as well as its derivative, $d\boldsymbol{\kappa}^c/d\omega$, are shown at the top of Fig. 5. From this figure, we clearly find that, in the α, β, and γ phases, the phonon modes with their frequencies up to ∼6, ∼12 and ∼10 THz largely contribute to the respective $\boldsymbol{\kappa}$. The frequencies shown in the contour maps in Fig. 4 are within these frequency ranges and thus we confirm that those bands significantly contribute to the $\boldsymbol{\kappa}$.

Assuming τ_λ and $\mathbf{v}_\lambda$ constant, then $d\kappa^c_{ii}/d\omega$ (ii=xx, zz) are proportional to phonon density of states (DOS)

$$g(\omega) = \frac{1}{N_{\mathbf{q}}\Omega}\sum_\lambda \delta(\omega-\omega_\lambda). \qquad (4)$$

In this context we view $g(\omega)$ as frequency distributions of heat carrier density. Alternatively, assuming only τ_λ

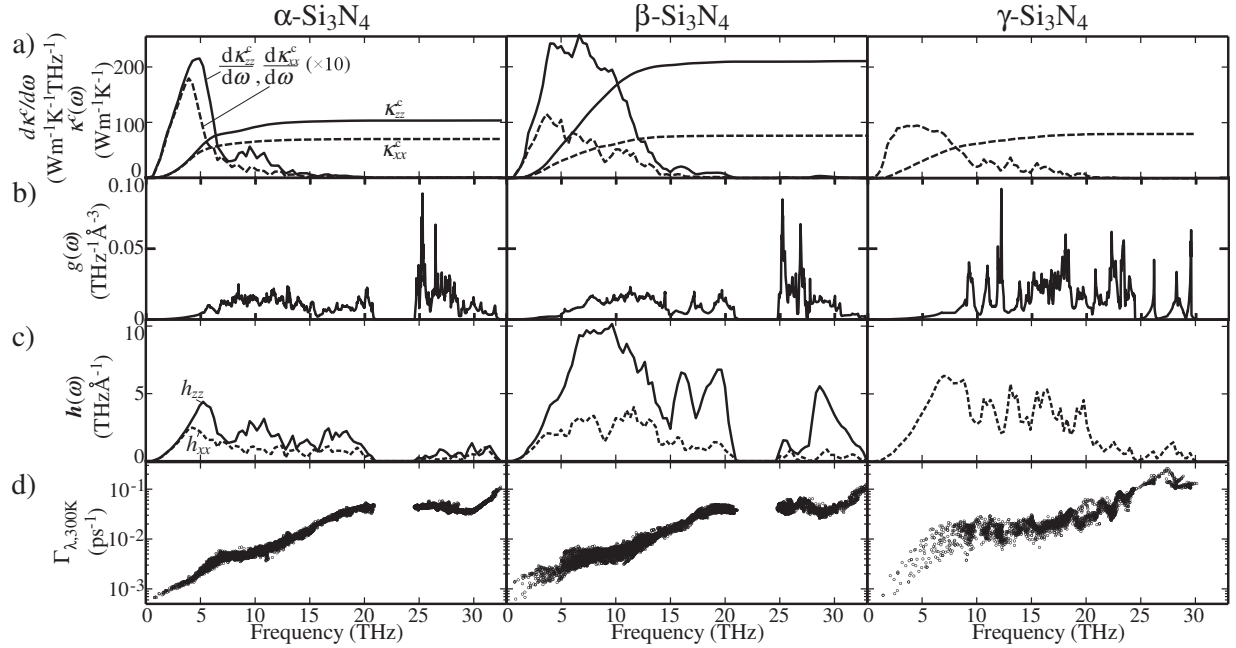

FIG. 5. (color online) Microscopic phonon properties of three Si_3N_4 phases. Cumulative thermal conductivity $\boldsymbol{\kappa}^{\rm c}$ and its frequency derivative (a), DOS as $g(\omega)$ (b), DOS weighted with $\mathbf{v}_\lambda \otimes \mathbf{v}_\lambda$ as $\boldsymbol{h}(\omega)$ (c), and scatter plots of linewidths and phonon frequencies, $(\Gamma_\lambda, \omega_\lambda)$, (d).

constant, then $d\boldsymbol{\kappa}^c/d\omega$ is proportional to

$$\boldsymbol{h}(\omega) = \frac{1}{N_{\mathbf{q}}\Omega}\sum_{\lambda} \mathbf{v}_\lambda \otimes \mathbf{v}_\lambda \delta(\omega - \omega_\lambda), \tag{5}$$

from which we examine the impacts of both of the $\mathbf{v}_\lambda$ and heat carrier density. $g(\omega)$ and $\boldsymbol{h}(\omega)$ are shown in Figs. 5-b and c. As for the frequency variation of $\tau_{\lambda,ph-ph}$, phonon linewidths are shown as scatter plots of $(\Gamma_\lambda, \omega_\lambda)$ in Fig. 5-d.

Comparing between the α and β phases, their linewidth distributions are qualitatively similar, except for a striking difference below ∼5 THz, which will be examined later. The markedly different $d\kappa^c_{ii}/d\omega$ between the two phases are therefore ascribed to the corresponding h_{ii}. Moreover, because the overall spectral shapes of $g(\omega)$ are also similar between the two phases, the $\mathbf{v}_\lambda$ alone accounts for the different behaviors of the $d\kappa^c_{ii}/d\omega$. Thus we conclude that the different anisotropy in $\boldsymbol{\kappa}$ is qualitatively explained by the different $\mathbf{v}_\lambda$, due to the folding effects of the band gaps and anticrossings. In contrast to this, in the case of the zincblende and wurtzite structures, the group velocities are suggested to be similar from their band structures[15], because the anticrossings are not created by the folding, as the optical branches are located at much higher frequencies than in the present system. This must result in the similar $\boldsymbol{\kappa}$ between these structures, irrespective of the stacking manners.

The γ phase has much different $g(\omega)$, $\boldsymbol{h}(\omega)$, and, Γ_λ from the others as expected from the large differences in the crystal structure. The most significant difference is in its phonon linewidths. Below ∼10 THz, they are approximately twice larger than those of the other phases. We will examine this details later. As a result, the $d\kappa^c_{xx}/d\omega$ shows relatively low intensities. Since the longitudinal acoustic phonon branch increases its frequencies much, as we have examined in the band diagram, $d\kappa^c_{xx}/d\omega$ rather gradually attenuates as frequency increases, occasionally resembling to $d\kappa^c_{xx}/d\omega$ of the β phase.

It is left curious that the linewidths are similar between the α and β phases although the group velocities show marked differences between them. In analogy to Lindsay *et al.*[44], we can say that Γ_λ in the present form depends on the phase space for the available two phonons, $\{\lambda', \lambda''\}$, and also depends on $|\Phi_{\lambda\lambda'\lambda''}|^2$. We examine these terms one-by-one. A distribution of two-phonon configurations is represented as a joint density of states (JDOS), $D_2(\mathbf{q}, \omega)$,

$$D_2(\mathbf{q},\omega) = D_2^{(1)}(\mathbf{q},\omega) + D_2^{(2)}(\mathbf{q},\omega) \tag{6}$$

where

$$\begin{aligned} D_2^{(1)} &= \frac{1}{N_{\mathbf{q}}Z^2}\sum_{\lambda'\lambda''} \Delta(-\mathbf{q}+\mathbf{q}'+\mathbf{q}'') \\ &\quad \times [\delta(\omega+\omega_{\lambda'}-\omega_{\lambda''}) + \delta(\omega-\omega_{\lambda'}+\omega_{\lambda''})], \\ D_2^{(2)} &= \frac{1}{N_{\mathbf{q}}Z^2}\sum_{\lambda'\lambda''} \Delta(-\mathbf{q}+\mathbf{q}'+\mathbf{q}'') \\ &\quad \times \delta(\omega-\omega_{\lambda'}-\omega_{\lambda''}), \end{aligned}$$

with $\Delta(\mathbf{x})$ giving 1 if $\mathbf{x}$ is a reciprocal lattice vector and otherwise zero. Z is the number of formula units in the

primitive unit cell and included as a scaling factor to compare JDOS for the structures with different Z. The equation of the linewidth in Eq. (1) contains terms of $(n_{\lambda'} + n_{\lambda''} + 1)$ and $(n_{\lambda'} - n_{\lambda''})$. Thus in more rigorous study, instead of $D_2^{(1)}$ and $D_2^{(2)}$, we should employ weighted JDOS with these terms. We firstly employ the JDOS in Eq. (6) to intuitively examine the similarity between the linewidths of the α and β phases. The weighted JDOS (WJDOS) will be briefly shown later including that of the γ phase.

Fig. 6 shows frequency-functions of JDOS at several different $\mathbf{q}$-points. They have very weak $\mathbf{q}$-point dependences. At the low frequency region up to $\simeq$ 10 THz $D_2^{(1)}$ is dominant between the two terms. The $D_2^{(1)}$ are similar between the phases. In the present Si_3N_4 system, the phonon modes of the acoustic and low-frequency optical branches, which largely contribute to the $\boldsymbol{\kappa}$, are much fewer than the other phonon modes. The JDOS are mainly determined by the latter majorities. As in the band diagrams, the branches of the majorities are rather flat. Thus we can approximately disregard in Eq. (6) the dependences of the $\omega_{\lambda'}$ and $\omega_{\lambda''}$ on the $\mathbf{q}'$ and $\mathbf{q}''$. In this case $D_2^{(1)}$ is simplified to the half part ($\omega \geq 0$) of the auto-correlation function of DOS. The DOS for both of the α and β phases in Fig. 5-a have a frequency gap. The $D_2^{(1)}$ reflect this DOS feature, dropping suddenly around 0 THz and showing a small shoulder around 5 THz, corresponding to the width of the gap. Because the gap is originated from the local modes of the planer NSi_3 composing each of the α and β crystal structures,[42] the $D_2^{(1)}$ are similar in these phases.

The WJDOS are shown in Fig. 7. The terms corresponding to $D_2^{(1)}$ and $D_2^{(2)}$ are denoted as $N_2^{(1)}$ and $N_2^{(2)}$. They are weighted $D_2^{(1)}$ and $D_2^{(2)}$ with $(n_{\lambda'} - n_{\lambda''})$ and $(n_{\lambda'} + n_{\lambda''} + 1)$, respectively. For the comparison among the three phases, we only show the frequency distributions at $\mathbf{q} = (0, 0, 0)$ because the $\mathbf{q}$ dependences of the WJDOS were as weak as JDOS. The weighting factors reduce the $N_2^{(1)}$ near 0 THz and enhance the $N_2^{(2)}$ in the high frequency range. The latter reduces the $d\boldsymbol{\kappa}^c/d\omega$ in the high frequency range, for all the phases. The total WJDOS are similar between the α and β phases. The γ phase has slightly small intensities of the total WJDOS below $\sim$10THz.

TABLE III. Averages of $|\Phi_{\lambda\lambda'\lambda''}|^2$ over frequency ranges of ω_λ (0–15 and 0–35 THz) and all (λ',λ'). The values are in units of 10^{-9} eV^{2}f.u.^{2}.

Frequency Range (THz)	Phase		
	α	β	γ
0–15	1.1	1.1	2.3
0–35	5.2	5.2	4.6

As for $|\Phi_{\lambda\lambda'\lambda''}|^2$, in Table. III, they are averaged over two kinds of frequency ranges of 0–15 or 0–35 THz for ω_λ and all indices in λ' and λ''. The averages are very similar values between the α and β phases. With the similar impacts of the (W)JDOS and $|\Phi_{\lambda\lambda'\lambda''}|^2$, the linewidths in these phases are similar. For the γ phase, the large $|\Phi_{\lambda\lambda'\lambda''}|^2$ attribute to the large linewidths. We set the frequency ranges for ω_λ so that the narrower frequency range approximately corresponds to the range where the phonon modes largely contribute to the $\boldsymbol{\kappa}$. A small change in the frequency ranges by a few THz did not change the qualitative characters of the averages.

Finally, we examine the exceptional, but striking difference in linewidth distributions between the α and β phases: In the α phase, Γ_λ below $\sim$5 THz are aligned on a single smooth line, while in the β phase, they are scattered roughly on two branches. This difference is investigated by trying to relate the linewidths with the directions of the atomic vibrations of the phonon modes.

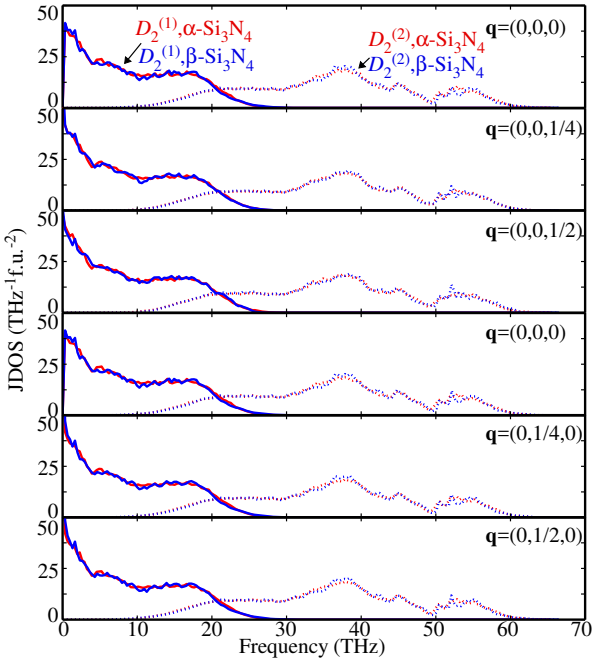

FIG. 6. (color online) JDOS of α- and β-Si_3N_4 at different $\mathbf{q}$ points. The first and forth rows are JDOS at the same Γ-point but calculated with the polarization for non-analytic term correction set along c^* and b^*, respectively.

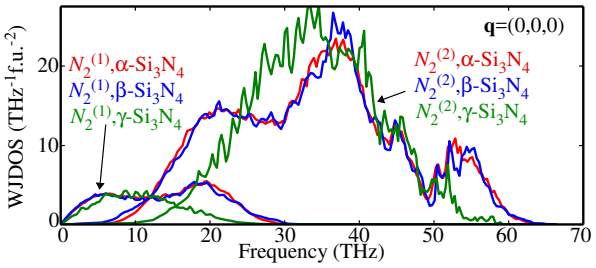

FIG. 7. (color online) Comparison of WJDOS at $\mathbf{q} = (0, 0, 0)$ for 300 K among the three phases.

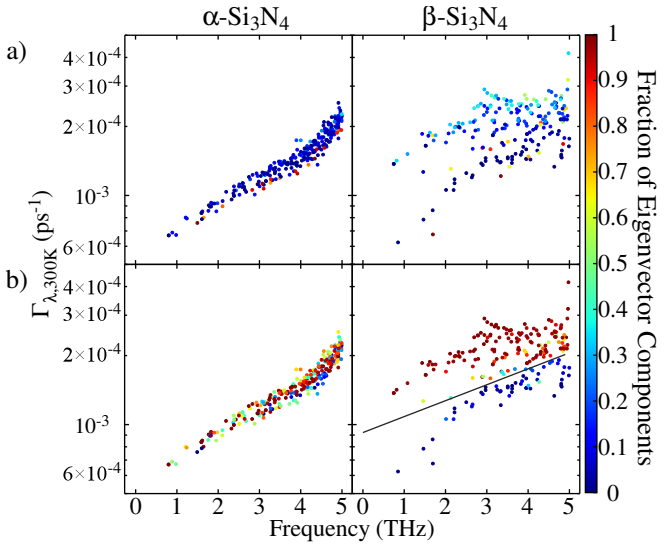

FIG. 8. (color online) Distribution of linewidths $\omega_\lambda \leq 5$ THz with colors with respect to strengths of eigenvector components along **q** (a) and on *ab* plane (b).

Fig. 8 enlarges the $(\Gamma_\lambda, \omega_\lambda)$ plots in this frequency range. In Fig. 8-a, the Γ_λ are classified using colors according to the sums of the squares of the eigenvector components along the **q**; the sum is 1 for a perfectly longitudinal wave. However, these sums show no clear contrast between the two branches in the β phase. Fig. 8-b shows the same plot as Fig. 8-a, but with colors according to the sums of the squares of the eigenvector components along the *ab* plane, which is 1 when the eigenvector lays on the *ab* plane. There is a tendency in the β phase that Γ_λ are large for atomic vibrations along the *ab* plane. This means that the vibration modes along the *ab* plane, belonging to the acoustic phonon branches, are more easily scattered in the β phase, no matter whether they are longitudinal or transverse. For the panel of β-Si_3N_4 in Fig. 8-b, a straight line splits the phonon modes to two groups. The numbers of the phonon modes assigned to the larger and smaller Γ_λ groups are 157 and 58, whose ratio is confirmed close to the population ratio of the vibration modes along and out of the *ab* plane.

IV. SUMMARY

In the present study, we investigate the lattice thermal conductivities of the three Si_3N_4 phases, by using the lattice dynamics based on the first principles interatomic force constants. The main remarks are as follows:

1) In the α- and β-Si_3N_4, whose crystal structures are characterized by the stacking manners of the basal layer structures, which largely alter $\boldsymbol{\kappa}$, due to the folding effects of the band gaps and anticrossings. This contrasts with the case of the zincblende and wurtzite structures in the previous study[15]. The $\boldsymbol{\kappa}$ of α-Si_3N_4 is rather isotropic, while the κ_{zz} of the β phase is twice or more larger than the other κ_{ii} of the three phases.

2) In the α phase, the acoustic mode phonons below 6 THz are the main heat carriers, while in the β phase, the phonons below 12 THz contribute to the $\boldsymbol{\kappa}$. Their group velocities are confirmed to characterize the behaviours of $\boldsymbol{\kappa}$.

3) In the γ phase, the frequency distribution of the phonon mode contributions to $\boldsymbol{\kappa}$ is similar to that for κ_{xx} of β-Si_3N_4. Its large phonon-phonon scattering strength and steep longitudinal acoustic branches attribute to this.

ACKNOWLEDGMENTS

The present work was partly supported by Grants-in-Aid for Scientific Research of MEXT, Japan (Grant No. 15K14108 and ESISM (Elements Strategy Initiative for Structural Materials) of Kyoto University).

Appendix A: Pressure dependence of lattice thermal conductivity of γ-phase

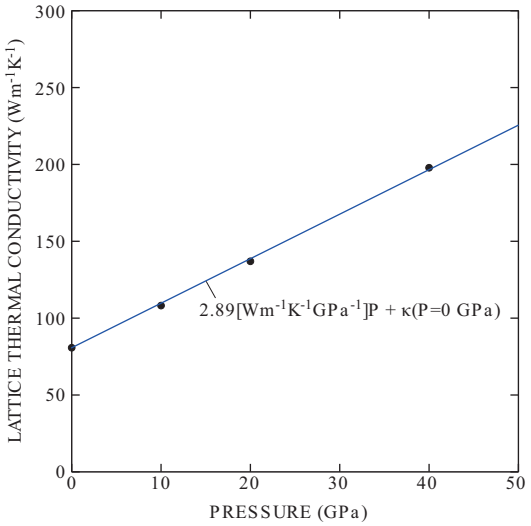

FIG. 9. (color online) Pressure dependence of lattice thermal conductivity of γ-Si_3N_4.

* k-tatsumi@imass.nagoya-u.ac.jp

[1] G. Slack, Journal of Physics and Chemistry of Solids **34**, 321 (1973).

[2] Y. Zhou, H. Hyuga, D. Kusano, Y.-i. Yoshizawa, and K. Hirao, Advanced Materials **23**, 4563 (2011).
[3] K. Hirao, K. Watari, H. Hayashi, and M. Kitayama, MRS Bulletin **26**, 451 (2001).
[4] K. Watari, Journal of the Ceramic Society of Japan **109**, S7 (2001).
[5] N. Hirosaki, Y. Okamoto, M. Ando, F. Munakata, and Y. Akimune, Journal of the Ceramic Society of Japan **104**, 49 (1996).
[6] N. Hirosaki, S. Ogata, C. Kocer, H. Kitagawa, and Y. Nakamura, Physical Review B **65**, 134110 (2002).
[7] F. L. Riley, Journal of the American Ceramic Society **83**, 245 (2000).
[8] M. Yashima, Y. Ando, and Y. Tabira, The Journal of Physical Chemistry B **111**, 3609 (2007).
[9] D. Du Boulay, N. Ishizawa, T. Atake, V. Streltsov, K. Furuya, and F. Munakata, Acta Crystallographica Section B: Structural Science **60**, 388 (2004).
[10] S. Hampshire, H. Park, D. Thompson, and K. Jack, Nature **274**, 880 (1978).
[11] T. Hahn, ed., International tables for crystallography, Vol. A (John Wiley & Sons, Inc., 2011).
[12] T. Hirai, S. Hayashi, and K. Niihara, AM. CERAM. SOC. BULL. Am. Ceram. Soc. Bull. **57**, 1126 (1978).
[13] B. Li, L. Pottier, J. Roger, D. Fournier, K. Watari, and K. Hirao, Journal of the european ceramic society **19**, 1631 (1999).
[14] R. Vashishta, R. K. Kalia, A. Nakano, and I. Ebbsö, Amorphous Insulators and Semiconductor, edited by M. F. Thorpe and M. I. Mitkova (Kluwer, 1996).
[15] A. Togo, L. Chaput, and I. Tanaka, Physical Review B **91**, 094306 (2015).
[16] A. Zerr, G. Miehe, G. Serghiou, M. Schwarz, E. Kroke, R. Riedel, H. Fueß, P. Kroll, and R. Boehler, Nature **400**, 340 (1999).
[17] Y. Zhang, A. Navrotsky, and T. Sekine, Journal of materials research **21**, 41 (2006).
[18] B. Xu, J. Dong, P. F. McMillan, O. Shebanova, and A. Salamat, Physical Review B **84**, 014113 (2011).
[19] D. Morelli and J. Heremans, Applied physics letters **81**, 5126 (2002).
[20] A. Togo and I. Tanaka, Scripta Materialia **108**, 1 (2015).
[21] L. Chaput, Physical review letters **110**, 265506 (2013).
[22] S.-i. Tamura, Physical Review B **27**, 858 (1983).
[23] P. E. Blöchl, Phys. Rev. B **50**, 17953 (1994).
[24] G. Kresse and J. Furthmüller, Physical review B **54**, 11169 (1996).
[25] G. Kresse, J. Non-Cryst. Solids **193**, 222 (1995).
[26] D. J. Kresse, Georg, Phys. Rev. B **59**, 1758 (1999).
[27] J. P. Perdew, K. Burke, and M. Ernzerhof, Phys. Rev. Lett. **77**, 3865 (1996).
[28] W. Paszkowicz, R. Minikayev, P. Piszora, M. Knapp, C. Bähtz, J. Recio, M. Marques, P. Mori-Sánchez, L. Gerward, and J. Jiang, Phys. Rev. B **69**, 052103 (2004).
[29] D. M. Ceperley and B. Alder, Physical Review Letters **45**, 566 (1980).
[30] S. Wei and M. Chou, Physical review letters **69**, 2799 (1992).
[31] Y. Wang, J. Wang, W. Wang, Z. Mei, S. Shang, L. Chen, and Z. Liu, J. Phys.: Condens. Matter **22**, 202201 (2010).
[32] M. Gajdoš, G. Hummer, G. Kresse, J. Furthmüller, and B. F, Phys. Rev. B **73**, 045112 (2006).
[33] X. Wu, D. Vanderbilt, and D. R. Hamann, Phys. Rev. B **72**, 035105 (2005).
[34] M. T. Dove, Introduction to lattice dynamics, Vol. 4 (Cambridge university press, 1993) pp. 76–77.
[35] A. Ward and D. Broido, Physical Review B **81**, 085205 (2010).
[36] R. Minikayev, W. Paszkowicz, P. Piszora, M. Knapp, and C. Bähtz, "Thermal expansion of and silicon nitride," (2007).
[37] W. Paszkowicz and R. Minikayev, Phys. Rev. B **69**, 052103 (2004).
[38] P. Andersson, Journal of Physics C: Solid State Physics **18**, 3943 (1985).
[39] A. Cepellotti and N. Marzari, Physical Review X **6**, 041013 (2016).
[40] R. J. Hardy, Physical Review B **2**, 1193 (1970).
[41] S. Mukhopadhyay, L. Lindsay, and D. J. Singh, Scientific reports **6** (2016).
[42] A. Kuwabara, K. Matsunaga, and I. Tanaka, Physical Review B **78**, 064104 (2008).
[43] W. E. Bies, R. J. Radtke, and E. H, J. Appl. Phys. **88**, 1498 (2000).
[44] L. Lindsay and D. A. Broido, J. Phys.: Condens. Matter **20**, 165209 (2008).